Strongly Quantum Confined Colloidal Cesium Tin Iodide Perovskite Nanoplates: Lessons for Reducing Defect Density and Improving Stability

Andrew Barnabas Wong,[†,‖] Yehonadav Bekenstein,[†,‖] Jun Kang,[‖] Christopher S. Kley,[†] Dohyung Kim,[‡] Natalie A. Gibson,[†,‖,⊥] Dandan Zhang,[†,‖] Yi Yu,[†,‖] Stephen R. Leone,[†,‖,⊥,§] Lin-Wang Wang,[‖] A. Paul Alivisatos,[†,‡,‖,#] and Peidong Yang*[,†,‡,‖,#]

[†]Department of Chemistry, [‡]Department of Materials Science and Engineering, and [§]Department of Physics, University of California, Berkeley, California 94720, United States

[‖]Materials Sciences Division and [⊥]Chemical Sciences Division, Lawrence Berkeley National Laboratory, Berkeley, California 94720, United States

[#]Kavli Energy NanoScience Institute, Berkeley, California 94720, United States

S *Supporting Information*

ABSTRACT: Within the last several years, metal halide perovskites such as methylammonium lead iodide, $CH_3NH_3PbI_3$, have come to the forefront of scientific investigation as defect-tolerant, solution-processable semiconductors that exhibit excellent optoelectronic properties. The vast majority of study has focused on Pb-based perovskites, which have limited applications because of their inherent toxicity. To enable the broad application of these materials, the properties of lead-free halide perovskites must be explored. Here, two-dimensional, lead-free cesium tin iodide, ($CsSnI_3$), perovskite nanoplates have been synthesized and characterized for the first time. These $CsSnI_3$ nanoplates exhibit thicknesses of less than 4 nm and exhibit significant quantum confinement with photoluminescence at 1.59 eV compared to 1.3 eV in the bulk. Ab initio calculations employing the generalized gradient approximation of Perdew−Burke−Ernzerhof elucidate that although the dominant intrinsic defects in $CsSnI_3$ do not introduce deep levels inside the band gap, their concentration can be quite high. These simulations also highlight that synthesizing and processing $CsSnI_3$ in Sn-rich conditions can reduce defect density and increase stability, which matches insights gained experimentally. This improvement in the understanding of $CsSnI_3$ represents a step toward the broader challenge of building a deeper understanding of Sn-based halide perovskites and developing design principles that will lead to their successful application in optoelectronic devices.

KEYWORDS: *Lead-free halide perovskites, all-inorganic halide perovskites, cesium tin iodide, nanoplates, defect tolerance*
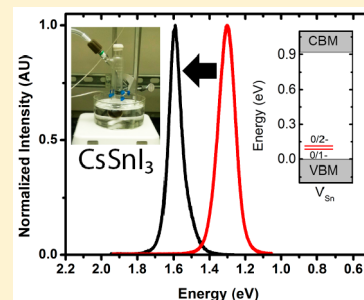
Defect-tolerant metal halide perovskites have revolutionized research toward solution-processable optoelectronics with photovoltaic (PV) efficiencies quickly exceeding 20%,[1−3] with light-emitting diodes (LEDs),[4] photodetectors,[5] and lasers[6] also reported. Metal halide perovskites span hybrid perovskites as well as all-inorganic halide perovskites, which have been proposed to offer stability advantages.[7] After Protesescu et al. introduced the colloidal synthesis of all-inorganic $CsPbX_3$ (X = Cl, Br, or I) nanocubes, a library of morphologies have been introduced including 0D nanocubes, 1D nanowires, and 2D nanoplates.[8−14] Going forward, the next step is to develop less-toxic lead-free halide perovskites.

The development of lead-free halide perovskites has been one of the key unmet challenges limiting the application of metal halide perovskites. One particularly intriguing all-inorganic composition is $CsSnI_3$, which has an unusual combination of semiconducting, metallic, and insulating bulk properties. Like lead halide perovskites, it exhibits photoluminescence (at 1.3 eV) and high mobility (~585 cm^2 V^{-1} s^{-1}), but counterintuitively, this material also exhibits high

electrical conductivity with a metallic temperature dependence.[15] High conductivity has been attributed to a high density of Sn vacancies that surprisingly does not lead to low mobility.[15] Recently, we demonstrated that $CsSnI_3$ nanowires also exhibit ultralow thermal conductivity of 0.38 ± 0.04 W m^{-1} K^{-1}.[16] It is a unique feature of $CsSnI_3$ that high electronic conductivity can exist in a thermally insulating single-crystalline material as these properties generally do not coexist. In addition, $CsSnI_3$ has been predicted to act as a topological insulator under pressure.[17] Overall, the study of $CsSnI_3$ nanostructures is of fundamental interest and is likely to lead to new insights.
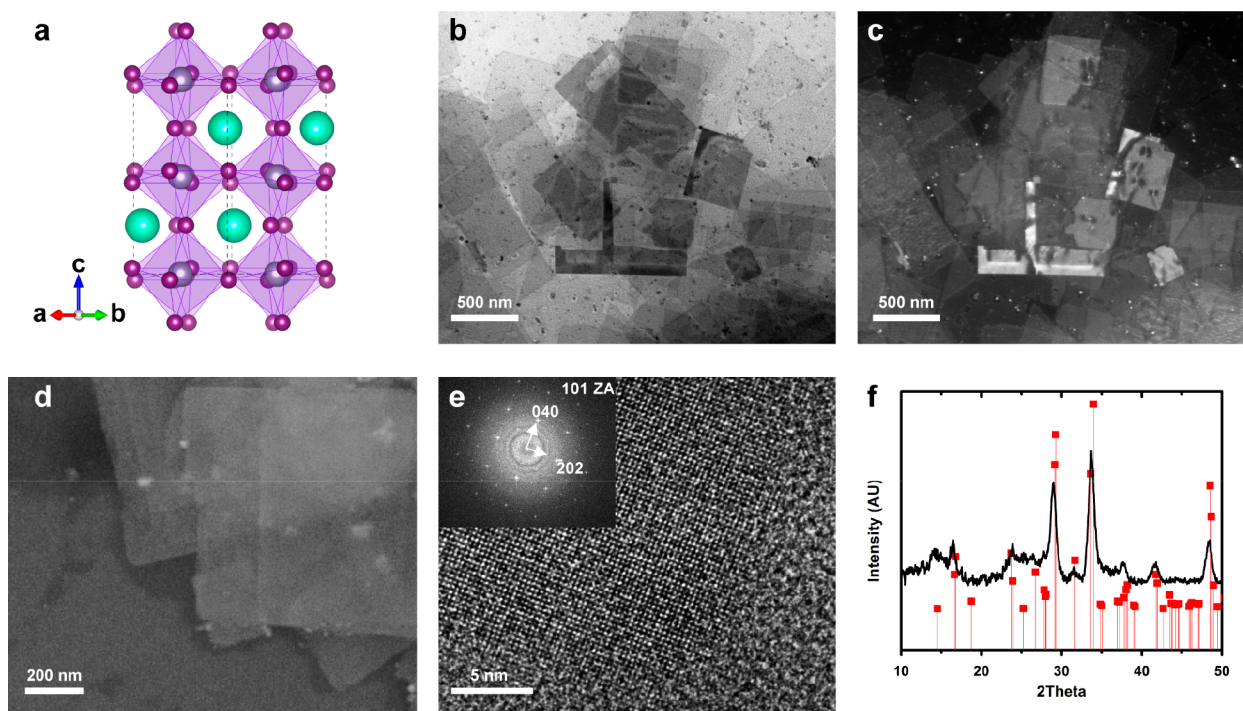
However, the study of $CsSnI_3$ is challenging because of poor stability.[15] The black, room-temperature orthorhombic phase, B-$CsSnI_3$, is a slight distortion of the cubic perovskite structure.

Figure 1. Structural characterization of $CsSnI_3$ nanoplates. (a) Crystal structure of orthorhombic, black $CsSnI_3$. Cs, Sn, and I atoms are shown in green, gray, and purple, respectively, with Sn–I octahedra shown in light purple. (b) Low-resolution TEM image of $CsSnI_3$ nanoplates. (c) DF-TEM image of $CsSnI_3$ nanoplates of the same region as in panel b. (d) SEM image of $CsSnI_3$ nanoplates deposited on a Si substrate. (e) HRTEM image of a $CsSnI_3$ nanoplate. Inset: FFT pattern corresponding to the [101] zone axis of $CsSnI_3$. (f) XRD pattern of $CsSnI_3$ nanoplates with the standard pattern of $CsSnI_3$ is shown in red.

In air, B-$CsSnI_3$ can oxidize, and it also transforms into a more-stable, nonperovskite polymorph of yellow $CsSnI_3$ that consists of $[Sn_2I_6^{2-}]$ double chains.[15] These stability issues create a challenge for the utilization of $CsSnI_3$, which would otherwise be an attractive alternative to other near-infrared (near-IR) direct band gap materials such as CdTe or GaAs. While $CsSnI_3$ has been used for near-IR lasers, LEDs, and PVs, stability has likely limited performance.[18−20] In principle, $CsSnI_3$ has excellent material properties for PVs, but $CsSnI_3$ absorber layers have only yielded 3.56% efficiency.[21−23] Recent work has shown that stability improves after adding $SnCl_2$ or SnF_2, which may act as passivation layers, and it has been reported that the use of reducing hydrazine vapor during device fabrication can improve performance by reducing Sn^{4+} defects.[20,22,24,25]

Efforts to improve stability further will benefit from a fundamental understanding of defects and stability in $CsSnI_3$. As recently demonstrated for $CsPbBr_3$ and hybrid perovskites,[26,27] calculations provide a systematic understanding of defect formation energies and defect charge transition levels based on the chemical potential region that stabilizes $CsSnI_3$. These analyses illustrate dominant types of defects and their influence on recombination. Previous studies separately calculated formation of Cs−Sn−I phases based on reactant chemical potential and calculated defect levels in $CsSnI_3$ in tin-poor/iodine-rich, cesium-poor/iodine-rich, and tin-rich/iodine-poor conditions.[15,28,29] There has been debate regarding whether deep-level defects dominate in $CsSnI_3$.[15,29] Further ab initio calculations are necessary to complement existing work and to compare more closely with experimental measurements for defect formation as well as to explore other fundamental properties, such as quantum confinement effects.

Strongly quantum confined and 2D $CsSnI_3$ nanostructures synthesized by a colloidal method have yet to be demonstrated. Recently, a colloidal synthesis of $CsSnX_3$ (X = Cl, Br, or I) nanocubes was reported by Jellicoe et al., although these nanocubes exhibited only very weak quantum confinement.[30] Hybrid organic−inorganic Sn-based perovskite systems also have been reported recently.[31,32] In particular, 2D structures represent an important morphology to understand quantum confinement in halide perovskites that affords a comparison between the theoretically predicted size dependence of confinement effects and experimental results.[33]

In this work, we developed the synthesis of strongly quantum confined 2D $CsSnI_3$ nanoplates by tuning the capping ligands used during catalyst-free colloidal synthesis, and we have performed ab initio calculations to investigate the defect-formation energies and defect charge-transition levels in $CsSnI_3$, which highlight the importance of Sn-rich synthesis and processing conditions to improve $CsSnI_3$ stability and minimize defect density. Furthermore, we have demonstrated experimentally using time-resolved photoluminescence studies that the contribution of a fast decay process is reduced when $CsSnI_3$ nanoplates are resuspended in Sn-rich instead of Sn-poor solutions, in agreement with our theoretical calculations.

The colloidal synthesis of $CsSnI_3$ nanoplates utilized standard air-free techniques (see the Supporting Information). For the synthesis of $CsSnI_3$ nanoplates, we utilized trioctylphosphine (TOP) both as a reducing agent and as a solvent to dissolve SnI_2 while minimizing oxidation. This solution was injected into a heated mixture of $CsCO_3$ with long- and short-chain amines (oleylamine and octylamine) and a short-chain organic acid (octanoic acid). A pair of predominant features of this synthesis are a combination of
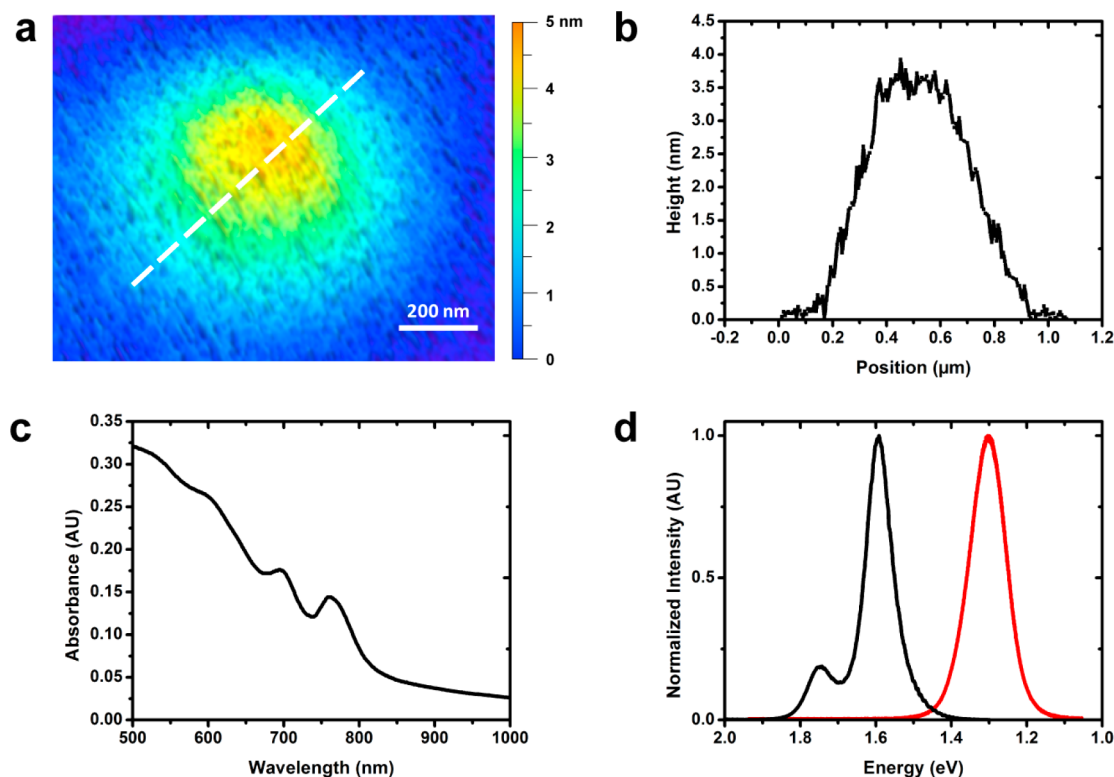
Figure 2. Confinement in CsSnI$_3$ studied by thickness measurements and optical characterization. (a) AFM image of a single CsSnI$_3$ nanoplate as measured in non-contact mode in an air-free cell. (b) AFM height profile across a single, isolated CsSnI$_3$ nanoplate as shown in panel b by the dashed line. (c) Absorbance spectrum of CsSnI$_3$ nanoplates. (d) Photoluminescence spectra of quantum-confined CsSnI$_3$ nanoplates (black) and bulk CsSnI$_3$ (red).

long- and short-chain ligands to control particle morphology as well as the use of TOP with high Sn concentrations. To achieve shape control of CsPbBr$_3$, the combination of long- and short-chain amines at reduced temperature is an effective strategy to control particle shape to produce platelets.[14] This empirical observation is consistent with the use of octylamine with oleylamine to direct the colloidal products to form CsSnI$_3$ nanoplates. The ratio of long- and short-chain amines and the use of a short-chain organic acid are very important for obtaining CsSnI$_3$ nanoplates in high yield (Figures S1 and S2), with octylamine and octanoic acid promoting the growth of large CsSnI$_3$ plates. Morphology seems less-sensitive to temperature (120 to 160 °C) and time (10 to 240 min), which is different than what has been observed in lead halide perovskites. (Figures S3 and S4).[8,11−14] Furthermore, the use of TOP as a mildly reducing solvent in this synthesis is reminiscent of hydrazine vapor reducing agent treatments of thin-film CsSnI$_3$ to prevent oxidation and the formation of Sn-based defects.[25] In contrast to previous reports,[30] we found that nucleation of B-CsSnI$_3$ can occur in the absence of TOP, if the organic solvents are very carefully dried as illustrated by transmission electron microscopy (TEM) and X-ray diffraction (XRD) (Figure S5 and S6). However, as demonstrated in this work, if TOP is employed with a large excess of SnI$_2$, the reaction is more-robust, and reaction conditions and morphology control are more tunable (see the Supporting Information for more details).

As shown in Figure 1, the dominant product of the colloidal synthesis is CsSnI$_3$ nanoplates with edge lengths of several hundred nanometers, which are in the room-temperature B-CsSnI$_3$ orthorhombic phase consisting of Sn−I octahedra

slightly reoriented relative to the ideal perovskite structure as illustrated in Figure 1a. As a result of the large edge lengths, these plates tend to stack because of strong interactions between organic capping layers (Figure 1b).[13,31,34,35] Dark-field TEM (DF-TEM) also provides a means by which to visualize stacked nanoplates while highlighting their crystallinity because the image is formed by imaging diffracted electrons from an ensemble of stacked CsSnI$_3$ nanoplates (Figures 1c and S7). As shown via scanning electron microscopy (SEM), overlapping CsSnI$_3$ plates are clearly distinguished at high and low magnification (Figures 1d and S8). Under these SEM imaging conditions, this sample is partially transparent, which is an indication of the formation of thin plates.

The composition of the nanoplates is confirmed by a combination of high-resolution TEM (HRTEM) and XRD. At the single nanoplate level, the lattice fringes can be clearly resolved via HRTEM with a reduced dose, as demonstrated in Figure 1e. As shown in the inset, the fast Fourier transform (FFT) pattern indicates that these nanoplates have the structure of black orthorhombic CsSnI$_3$ laying along its [101] zone axis. Furthermore, as illustrated in Figure 1f, the XRD of the purified nanoplate sample sealed in an air-free holder also confirms the assignment of the structure, as shown by the red dropdown lines of the B-CsSnI$_3$ standard pattern (ICSD no. 69996). In addition, energy dispersive X-ray spectroscopy also confirms the stoichiometry of the CsSnI$_3$ nanoplates (Figures S9 and S10).

An important consideration is the thickness of these 2D sheets, which dictates the extent of quantum confinement. Atomic force microscopy (AFM) was performed in noncontact mode in an air-free cell to estimate the thickness of CsSnI$_3$

nanoplates, as shown in Figure 2a, which allows a height profile to be extracted (Figure 2b). As is the case in examples of AFM on colloidal $CsPbBr_3$ nanoplates, the edges of the profile are rounded due to ligand tip interactions.[12,14] Nevertheless, the height of the nanoplate with its ligand shell is estimated to be 3.8 nm, which corresponds to 4 or 5 layers of black-phase orthorhombic $CsSnI_3$ in the [101] direction depending on the effective thickness and packing of the ligand shell on the washed $CsSnI_3$ nanoplate. These are the thinnest $CsSnI_3$ nanoplatelets reported so far and are expected to exhibit a high degree of quantum confinement.

For the previously reported $CsSnI_3$ nanocubes with edge lengths of 9.9 nm, the photoluminescence only shifted from the bulk value of 950 nm to about 920 nm (0.03 eV),[30] which is similar to weakly confined $CsPbBr_3$ nanocubes relative to bulk $CsPbBr_3$.[8,12] Recently, the related organic–inorganic hybrid Sn-based systems $L_2[SnI_4]$ (where L is octylammonium or butylammonium) and $L_2[FASnI_3]SnI_4$ (where FA is formamidinium) were reported to have blue-shifts of 0.7 and 0.4 eV, respectively, relative to bulk $FASnI_3$.[31] Based on the absorbance and photoluminescence spectra in Figures 2c and 2d, respectively, the band edge has blue-shifted to 780 nm (1.59 eV), which is 0.29 eV from the photoluminescence of bulk $CsSnI_3$ (red), indicating that these nanoplates are strongly quantum confined to a similar extent as several unit cell thick $CsPbBr_3$ nanoplates.[12] Strong dielectric confinement in these thin nanoplates also increases electron–hole interactions, which lead to a highly excitonic character of the band edge that is evident in the sharp peak in the absorbance spectrum.[33] Here, the absorbance spectrum shows excitonic character similar to the case of highly confined lead halide perovskite nanocrystals.[8,12,33,36] In some cases, a second population of nanoplates can emit at 710 nm (1.74 eV), which may correspond to approximately one layer thinner $CsSnI_3$ nanoplates with a blueshift of 0.44 eV (Figure S11), which is similar to reports for $CsPbBr_3$ nanoplates with different thicknesses.[12] However, in this work, we did not explore the tunability of the thickness of the 2D $CsSnI_3$ nanoplates. According to ab initio simulations using a Heyd–Scuseria–Ernzerhof (HSE) functional with spin–orbital coupling correction, it is predicted that the band gap of $CsSnI_3$ nanoplates should blue-shift by 0.887 to 0.418 eV for plates that are 1 to 5 layers thick in the [101] direction, respectively, versus the bulk (see the Supporting Information for calculation details). It is important to note that this calculation of the band gap does not include exciton binding energy, which will cause a red shift in the observed emission and absorption. Here, the magnitudes of the simulated values for the band gap of confined $CsSnI_3$ are in agreement with the experimentally observed blueshifts in $CsSnI_3$. Another quantity that we can observe is the Stokes shift based on the energies of the maximum absorption and maximum emission, which is approximately 30 meV for these confined $CsSnI_3$ nanoplates. This value is in the range previously observed for strongly confined $CsPbBr_3$ nanostructures.[8,36]

A clear difference between the lead halide and tin halide perovskites is their sensitivity to synthetic conditions. While almost any synthetic condition will grow material with high photoluminescence quantum efficiency for the lead-based systems, the Sn-based systems are more complex.[15,18,20,30] An improved understanding of the energetics of intrinsic point defects in $CsSnI_3$ yields valuable insights on the formation of these defects and the properties of this material under different synthetic conditions. To that end, we employed ab initio

calculations using the generalized gradient approximation of Perdew–Burke–Ernzerhof (GGA-PBE). The calculated band structure of the black, orthorhombic phase of $CsSnI_3$ is shown in Figure 3a with and without spin–orbit coupling with a direct
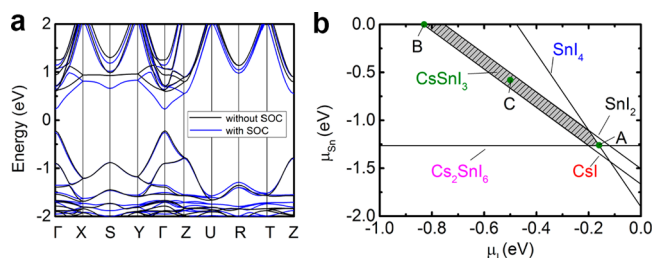
Figure 3. Ab initio calculations of the electronic structure and calculated conditions for stabilizing $CsSnI_3$. (a) Calculated band structure of $CsSnI_3$ with and without spin–orbit coupling (blue and black, respectively). (b) Stability regions of Cs, Sn, and I compounds against Sn and I chemical potentials. $\mu = 0$ corresponds to bulk I or Sn, and the shaded region corresponds to the stability region for the synthesis of $CsSnI_3$.

band gap at the Γ point, which is in agreement with recent reports.[15,16] The relative stability of the black, orthorhombic phase of $CsSnI_3$ against other Cs/Sn/I compounds depends on the chemical potential, μ, of the constituent elements. In Figure 3b, we present the calculated chemical potential region in which $CsSnI_3$ is stable under equilibrium growth conditions (see the Supporting Information for detailed methods). This region constricts the possible μ values of constituent elements. It should be noted that the $\mu = 0$ in Figure 3b corresponds to bulk I or Sn. Points A–C in Figure 3b correspond to I-rich, Sn-rich, and moderate growth conditions, respectively. We have considered all possible intrinsic point defects in $CsSnI_3$, namely antisites (I_{Cs}, I_{Sn}, Cs_{Sn}, Cs_I, Sn_{Cs}, and Sn_I), interstitials (Cs_i, Sn_i, and I_i), and vacancies (V_{Cs}, V_{Sn}, and V_I). The formation energies of the defects at each point A–C were calculated as detailed in the Supporting Information, and the results are tabulated in Table 1.
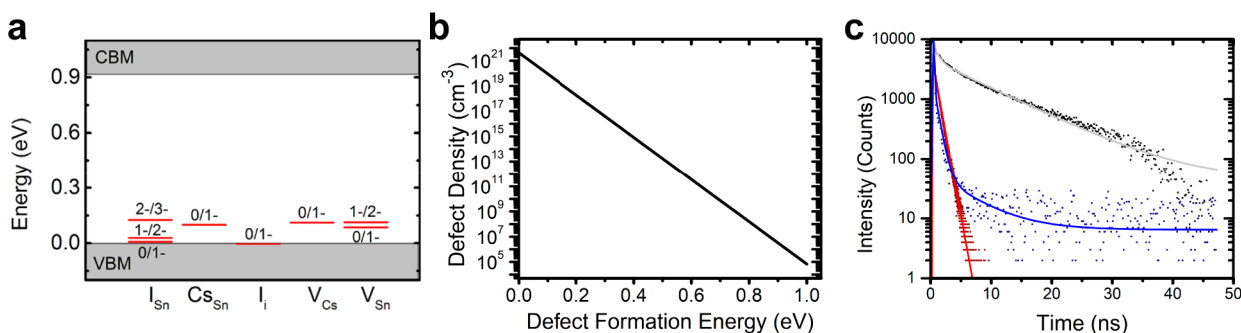
Based on the calculated defect formation energies, we can see that Cs_{Sn}, I_i, V_{Cs}, and V_{Sn} for all growth conditions (A–C) possess defect formations less than 1 eV, with I_{Sn} also possessing a formation energy of less than 1 eV for condition A (I-rich). In good agreement with a previous report, Sn vacancies tend to have the lowest defect formation energy in all cases out of all possible point defects.[15] Thus, V_{Sn} is the dominant defect in $CsSnI_3$. In our calculations, the formation energy of V_{Sn} is actually negative for conditions A and C, which suggests that these defects can form with an extremely high density. A negative energy of formation is also predicted for V_{Cs} under condition A. Table 1 also demonstrates that the Sn-rich growth condition (point B) leads to higher formation energies of these defects, which can help to reduce the defect concentration, as will be discussed later.

For the defects with formation energies less than 1 eV, the charge transition levels of the defects within the band gap are calculated using the generalized gradient approximation of Perdew–Burke–Ernzerhof (GGA-PBE) without spin–orbit coupling, and these results are plotted in Figure 4a. It is seen that all these defects introduce acceptor levels close to the valence band maximum (VBM). It is important to note that very deep-level traps are not present, which shows that $CsSnI_3$

Table 1. Formation Energies of Defects in CsSnI$_3$ at Different Points (A, B, and C) in the Chemical Potential Diagram in Figure 3b^a

	I_{Cs}	I_{Sn}	Cs_{Sn}	Cs_I	Sn_{Cs}	Sn_I	Cs_i	Sn_i	I_i	V_{Cs}	V_{Sn}	V_I
A	1.06	**0.84**	**0.10**	3.54	1.85	3.97	2.12	3.51	**0.26**	**-0.17**	**-0.72**	1.68
B	2.48	2.77	**0.61**	2.52	1.34	2.04	1.37	2.25	**0.93**	**0.58**	**0.54**	1.01
C	1.74	1.86	**0.44**	3.26	1.51	2.95	1.78	2.83	**0.60**	**0.17**	**-0.04**	1.34

^{a}Formation energies of less than 1 eV are shown in bold.

Figure 4. Impact of defects in CsSnI$_3$ as described theoretically and experimentally. (a) Calculated defect charge-transition levels within the band gap of CsSnI$_3$. Defects plotted have a formation energy less than 1 eV. (b) Calculated defect density as a function of defect formation energy in CsSnI$_3$. (c) Experimental TRPL measurements of CsSnI$_3$ nanoplates with (black) and without (navy blue) treatment with SnI$_2$ complexes as well as bulk CsSnI$_3$ (dark red). Fitted curves are shown in gray, blue, and red, respectively.

is defect tolerant in this sense. Nevertheless, defects such as V$_{Sn}$ can form with high density based on the low formation energy.

The finding that CsSnI$_3$ has the lowest (and potentially negative) energy for the formation of V$_{Sn}$ has important consequences for the best practices to synthesize this material for applications in optoelectronic devices. Because V$_{Sn}$ has a low or negative formation energy, a very high concentration of shallow acceptor levels is expected from V$_{Sn}$. As a consequence, the black orthorhombic phase of CsSnI$_3$ should exhibit high p-type electrical conductivity and low photoluminescence quantum efficiency based on a high carrier density, which enhances nonradiative recombination processes such as Auger recombination and causes high structural instability because vacancy sites can reduce the barrier for structural rearrangements.[37] Therefore, a high density of vacancies leading to instability and facile rearrangement to the nonperovskite yellow orthorhombic phase partially explains the difficulty in synthesizing and handling CsSnI$_3$. A high density of Sn vacancies in CsSnI$_3$ may also partly explain photoluminescence quantum efficiency measurements much less than 1% as well as photovoltaic efficiencies less than 4%.[22,23,30] As conditions become increasingly Sn-deficient, Cs$_2$SnI$_6$ will form, as illustrated in Figure 3b.[38]

Based on these results, to improve the quality and stability of CsSnI$_3$ for applications in optoelectronic devices, new extremely Sn-rich conditions for synthesizing and handling CsSnI$_3$ should be explored with the chemical potential of Sn as close as possible to Sn metal to increase the formation energies of the dominant point defects and decrease defect density. The density of point defects in CsSnI$_3$ can be estimated based on their formation energy as plotted in Figure 4b. The increase in the formation energy of defects such as V$_{Sn}$ has a dramatic impact on the defect density, which highlights the importance of minimizing defect formation energy during synthesis and handling of CsSnI$_3$.

If these Sn-rich conditions can be developed experimentally without inducing other types of defects, the density of V$_{Sn}$

should be much lower, so stability and photoluminescence quantum efficiency should be improved. In addition, another potential stabilization strategy that has been implemented in CsPbI$_3$ nanocrystals is to alloy with another element to introduce strain and alter the cohesive energy in a way that can prevent structural rearrangements to the nonperovskite polymorph phase.[39] It may also be possible to develop analogous strategies to stabilize CsSnI$_3$ by alloying the nanocrystals to prevent reorganization to the nonperovskite yellow-phase CsSnI$_3$ polymorph and to alter the energetics to disfavor defect formation. However, such a strategy would also need to avoid introducing new deep-level trap states as a result of the introduction of the alloying material itself.

From an experimental point of view, we have sought to explore the impact of treatment in Sn-rich conditions on stability and carrier dynamics in CsSnI$_3$ nanoplates, as suggested by our computational work. It should be noted that the high surface area of the CsSnI$_3$ nanoplate sample leaves it vulnerable to sample degradation by multiple routes that have been observed in halide perovskite nanoplates, and the improvement of the stability is an important consideration in this class of materials.[33] When the purified CsSnI$_3$ nanoplates were resuspended in anhydrous hexane that was dried by molecular sieves, the dark solution had a tendency to lighten over time as the CsSnI$_3$ nanoplates degraded. It was found that treating 1 mL of hexane with 10 μL of 1 M SnI$_2$ dissolved in TOP dramatically slowed the degradation of CsSnI$_3$ nanoplates resuspended in anhydrous hexane, which is illustrated by comparing the absorption and photoluminescence emission of the sample several hours after suspending the nanoplates in hexane (Figure S12). The ab initio calculations presented in Table 1 suggest that the SnI$_2$-complex treatment stabilizes the nanoplates by increasing the formation energy of defects, such as V$_{Sn}$, by increasing μ$_{Sn}$ toward point B in Figure 3b in an analogous way to the role of SnF$_2$ in spin-coated CsSnI$_3$.[20] This would reduce the defect density, as shown in Figure 4b, and appears to improve the stability of the CsSnI$_3$ nanoplates.

To better understand the role of defects on the charge carrier dynamics in quantum confined $CsSnI_3$ nanoplates, we studied the time-resolved photoluminescence (TRPL) of nanoplates with different processing conditions after the same synthesis conditions. As shown in Figure 4c, the room temperature TRPL of untreated $CsSnI_3$ nanoplates (dark blue points and blue fitted curve) and Sn-treated nanoplates (black points and gray fitted curve) were measured under inert atmosphere. In addition, TRPL was performed on bulk $CsSnI_3$ microplate crystals (dark red points and red fitted curve) that were synthesized via the direct reaction of CsI with SnI_2 in anhydrous 2-propanol, as recently reported.[16] The parameters from curve fitting are tabulated in Table S1. The Sn-treated $CsSnI_3$ nanoplates exhibit significantly longer photoluminescence as compared to the bulk $CsSnI_3$ microplates and the untreated $CsSnI_3$ nanoplates. The Sn-treated nanoplates TRPL intensity could be fit to a biexponential with lifetimes of 0.81 ± 0.04 and 8.93 ± 0.12 ns for τ_1 and τ_2, respectively, with a weighting of 47% on τ_1 and 53% on τ_2 (gray curve). Similarly, the photoluminescence lifetime of the untreated $CsSnI_3$ nanoplates was fit to a biexponential with lifetimes of 0.72 ± 0.04 and 5.65 ± 3.11 ns for τ_1 and τ_2, respectively. Although the faster and slower lifetimes of the photoluminescence are similar for the treated and untreated cases, the weighting is very different. For the untreated nanoplates, the time constants for photoluminescence were weighted as 97% on τ_1 and 3% on τ_2 (blue curve), which is very different to the case of the Sn-treated $CsSnI_3$ nanoplates. The microplate photoluminescence lifetime is best fit to a monoexponential function with a τ_1 value of 0.79 ns (red curve), which is also similar to the shorter time constant for the treated and untreated nanoplates.

The qualitative difference in the decay kinetics can be motivated by the theoretical understanding of the defect structures from ab initio simulations. It appears that $CsSnI_3$ nanoplates have an intrinsic lifetime, τ_1, between ~0.7 to 0.8 ns. Given that the formation energy of V_{Sn} is the lowest in all growth conditions studied, it appears likely that the presence of V_{Sn} or similar defects may account for the fast, τ_1, lifetime. The treatment with dissolved SnI_2 appears to reduce the amount of decay that occurs via the fast lifetime, which extends the overall of the photoluminescence lifetime so that the slower τ_2 lifetime makes a greater contribution after treatment. This suggests that treatment with excess dissolved SnI_2 may reduce the density of defects such as V_{Sn}. This effect is in addition to the improvement in the stability of the suspended $CsSnI_3$ nanoplates as mentioned previously. It is important to note that we observed photoluminescence quantum yields less than 1% in both treated and untreated cases, which is not unexpected given previous reports of very low photoluminescence in colloidal $CsSnI_3$ and given that colloidal halide perovskite nanoplates often exhibit lower photoluminescence quantum yields than other morphologies.[30,33] Nevertheless, it seems likely that the treatment with dissolved SnI_2 increases the formation energy of defects, as shown in Table 1, which reduces defect density. In contrast to the nanoplates, the $CsSnI_3$ microplates were synthesized in 2-propanol with CsI and SnI_2 under a relatively low concentration of Sn, and this sample exhibits the fastest reduction in photoluminescence. Therefore, the dominance of a relatively faster lifetime in the photoluminescence seems to be related to processing and handling in Sn-poor environments. This is especially relevant to the stabilization of Sn-based halide perovskites and may also provide a means by which to improve the photoluminescence quantum yield.

In summary, strongly quantum confined, 2D $CsSnI_3$ nanoplates were synthesized and characterized, advancing the understanding of this important all-inorganic lead-free perovskite. Our analysis of the defect formation energies demonstrates that this material is more likely to form a high density of shallow trap states rather than deep trap states in agreement with our experiments. Formation of trap states and phase instabilities can be reduced by using Sn-rich conditions for synthesis and processing of $CsSnI_3$. New paradigms in the synthesis of these lead-free halide perovskites are likely necessary to further improve stability, reduce defect density, and improve parameters such as photoluminescence efficiency that would turn $CsSnI_3$ into a mainstream material capable of producing robust, high-performance optoelectronic devices.

■ ASSOCIATED CONTENT

Ⓢ Supporting Information

The Supporting Information is available free of charge on the ACS Publications website at DOI: 10.1021/acs.nanolett.8b00077.

Experimental details, calculations, and additional figures including TEM, XRD, SEM, EDS, and photoluminescence data. (PDF)

■ AUTHOR INFORMATION

Corresponding Author

*E-mail: p_yang@berkeley.edu.

ORCID Ⓞ

Andrew Barnabas Wong: 0000-0002-0731-1931

Yehonadav Bekenstein: 0000-0001-6230-5182

Jun Kang: 0000-0003-4788-0028

Dohyung Kim: 0000-0003-0201-9082

Yi Yu: 0000-0003-4326-5992

Stephen R. Leone: 0000-0003-4006-2292

A. Paul Alivisatos: 0000-0001-6895-9048

Peidong Yang: 0000-0003-4799-1684

Author Contributions

The manuscript was written through contributions of all authors. All authors have given approval to the final version of the manuscript. A.B.W. and Y.B. contributed equally.

Notes

The authors declare no competing financial interest.

■ REFERENCES

(1) Lee, M. M.; Teuscher, J.; Miyasaka, T.; Murakami, T. N.; Snaith, H. J. *Science* **2012**, *338*, 643−647.

(2) Burschka, J.; Pellet, N.; Moon, S.-J.; Humphry-Baker, R.; Gao, P.; Nazeeruddin, M. K.; Gratzel, M. *Nature* **2013**, *499*, 316−319.

(3) Zhou, H.; Chen, Q.; Li, G.; Luo, S.; Song, T.-B.; Duan, H.-S.; Hong, Z.; You, J.; Liu, Y.; Yang, Y. *Science* **2014**, *345*, 542−546.

(4) Tan, Z.-K.; Moghaddam, R. S.; Lai, M. L.; Docampo, P.; Higler, R.; Deschler, F.; Price, M.; Sadhanala, A.; Pazos, L. M.; Credgington, D.; Hanusch, F.; Bein, T.; Snaith, H. J.; Friend, R. H. *Nat. Nanotechnol.* **2014**, *9*, 687−692.

(5) Dou, L.; Yang, Y. M.; You, J.; Hong, Z.; Chang, W.-H.; Li, G.; Yang, Y. *Nat. Commun.* **2014**, *5*, 5404.

(6) Eaton, S. W.; Lai, M.; Gibson, N. A.; Wong, A. B.; Dou, L.; Ma, J.; Wang, L. W.; Leone, S. R.; Yang, P. *Proc. Natl. Acad. Sci. U. S. A.* **2016**, *113*, 1993−1998.

(7) Kulbak, M.; Cahen, D.; Hodes, G. *J. Phys. Chem. Lett.* **2015**, *6*, 2452−2456.

(8) Protesescu, L.; Yakunin, S.; Bodnarchuk, M. I.; Krieg, F.; Caputo, R.; Hendon, C. H.; Yang, R. X.; Walsh, A.; Kovalenko, M. V. *Nano Lett.* **2015**, *15*, 3692−3696.

(9) Park, Y.-S.; Guo, S.; Makarov, N.; Klimov, V. I. *ACS Nano* **2015**, *9*, 10386−10393.

(10) Swarnkar, A.; Chulliyil, R.; Ravi, V. K.; Irfanullah, M.; Chowdhury, A.; Nag, A. *Angew. Chem., Int. Ed.* **2015**, *54*, 15424−15428.

(11) Zhang, D.; Eaton, S. W.; Yu, Y.; Dou, L.; Yang, P. *J. Am. Chem. Soc.* **2015**, *137*, 9230−9233.

(12) Bekenstein, Y.; Koscher, B. A.; Eaton, S. W.; Yang, P.; Alivisatos, A. P. *J. Am. Chem. Soc.* **2015**, *137*, 16008−16011.

(13) Shamsi, J.; Dang, Z.; Bianchini, P.; Canale, C.; Di Stasio, F.; Brescia, R.; Prato, M.; Manna, L. *J. Am. Chem. Soc.* **2016**, *138*, 7240−7243.

(14) Pan, A.; He, B.; Fan, X.; Liu, Z.; Urban, J. J.; Alivisatos, A. P.; He, L.; Liu, Y. *ACS Nano* **2016**, *10*, 7943−7954.

(15) Chung, I.; Song, J.-H.; Im, J.; Androulakis, J.; Malliakas, C. D.; Li, H.; Freeman, A. J.; Kenney, J. T.; Kanatzidis, M. G. *J. Am. Chem. Soc.* **2012**, *134*, 8579−8587.

(16) Lee, W.; Li, H.; Wong, A. B.; Zhang, D.; Lai, M.; Yu, Y.; Kong, Q.; Lin, E.; Urban, J. J.; Grossman, J. C.; Yang, P. *Proc. Natl. Acad. Sci. U. S. A.* **2017**, *114*, 8693−8697.

(17) Jin, H.; Im, J.; Freeman, A. *Phys. Rev. B: Condens. Matter Mater. Phys.* **2012**, *86*, 121102.

(18) Xing, G.; Kumar, M. H.; Chong, W. K.; Liu, X.; Cai, Y.; Ding, H.; Asta, M.; Grätzel, M.; Mhaisalkar, S.; Mathews, N.; Sum, T. C. *Adv. Mater.* **2016**, *28*, 8191−8196.

(19) Hong, W.-L.; Huang, Y.-C.; Chang, C.-Y.; Zhang, Z.-C.; Tsai, H.-R.; Chang, N.-Y.; Chao, Y.-C. *Adv. Mater.* **2016**, *28*, 8029−8036.

(20) Kumar, M. H.; Dharani, S.; Leong, W. L.; Boix, P. P.; Prabhakar, R. R.; Baikie, T.; Shi, C.; Ding, H.; Ramesh, R.; Asta, M.; Grätzel, M.; Mhaisalkar, S. G.; Mathews, N. *Adv. Mater.* **2014**, *26*, 7122−7127.

(21) Chung, I.; Lee, B.; He, J.; Chang, R. P. H.; Kanatzidis, M. G. *Nature* **2012**, *485*, 486−489.

(22) Marshall, K. P.; Walker, M.; Walton, R. I.; Hatton, R. A. *Nat. Energy* **2016**, *1*, 16178.

(23) Chen, Z.; Yu, C.; Shum, K.; Wang, J. J.; Pfenninger, W.; Vockic, N.; Midgley, J.; Kenney, J. *J. Lumin.* **2012**, *132*, 345−349.

(24) Kontos, A. G.; Kaltzoglou, A.; Siranidi, E.; Palles, D.; Angeli, G. K.; Arfanis, M. K.; Psycharis, V.; Raptis, Y. S.; Kamitsos, E. I.; Trikalitis,

P. N.; Stoumpos, C. C.; Kanatzidis, M. G.; Falaras, P. *Inorg. Chem.* **2017**, *56*, 84−91.

(25) Song, T.-B.; Yokoyama, T.; Stoumpos, C. C.; Logsdon, J.; Cao, D. H.; Wasielewski, M. R.; Aramaki, S.; Kanatzidis, M. G. *J. Am. Chem. Soc.* **2017**, *139*, 836−842.

(26) Kang, J.; Wang, L.-W. *J. Phys. Chem. Lett.* **2017**, *8*, 489−493.

(27) Buin, A.; Comin, R.; Xu, J.; Ip, A. H.; Sargent, E. H. *Chem. Mater.* **2015**, *27*, 4405−4412.

(28) Xiao, Z.; Zhou, Y.; Hosono, H.; Kamiya, T. *Phys. Chem. Chem. Phys.* **2015**, *17*, 18900−18903.

(29) Xu, P.; Chen, S.; Xiang, H.-J.; Gong, X.-G.; Wei, S.-H. *Chem. Mater.* **2014**, *26*, 6068−6072.

(30) Jellicoe, T. C.; Richter, J. M.; Glass, H. F. J.; Tabachnyk, M.; Brady, R.; Dutton, S. E.; Rao, A.; Friend, R. H.; Credgington, D.; Greenham, N. C.; Böhm, M. L. *J. Am. Chem. Soc.* **2016**, *138*, 2941−2944.

(31) Weidman, M. C.; Seitz, M.; Stranks, S. D.; Tisdale, W. A. *ACS Nano* **2016**, *10*, 7830−7839.

(32) Liao, Y.; Liu, H.; Zhou, W.; Yang, D.; Shang, Y.; Shi, Z.; Li, B.; Jiang, X.; Zhang, L.; Quan, L. N.; Quintero-Bermudez, R.; Sutherland, B. R.; Mi, Q.; Sargent, E. H.; Ning, Z. *J. Am. Chem. Soc.* **2017**, *139*, 6693−6699.

(33) Weidman, M. C.; Goodman, A. J.; Tisdale, W. A. *Chem. Mater.* **2017**, *29*, 5019−5030.

(34) Lv, L.; Xu, Y.; Fang, H.; Luo, W.; Xu, F.; Liu, L.; Wang, B.; Zhang, X.; Yang, D.; Hu, W.; Dong, A. *Nanoscale* **2016**, *8*, 13589−13596.

(35) Wang, K.-H.; Wu, L.; Li, L.; Yao, H.-B.; Qian, H.-S.; Yu, S.-H. *Angew. Chem., Int. Ed.* **2016**, *55*, 8328−8332.

(36) Brennan, M. C.; Herr, J. E.; Nguyen-Beck, T. S.; Zinna, J.; Draguta, S.; Rouvimov, S.; Parkhill, J.; Kuno, M. *J. Am. Chem. Soc.* **2017**, *139*, 12201−12208.

(37) Sun, Z.; Zhou, J.; Pan, Y.; Song, Z.; Mao, H.-K.; Ahuja, R. *Proc. Natl. Acad. Sci. U. S. A.* **2011**, *108*, 10410−10414.

(38) Dolzhnikov, D. S.; Wang, C.; Xu, Y.; Kanatzidis, M. G.; Weiss, E. A. *Chem. Mater.* **2017**, *29*, 7901−7907.

(39) Akkerman, Q. A.; Meggiolaro, D.; Dang, Z.; De Angelis, F.; Manna, L. *ACS Energy Lett.* **2017**, *2*, 2183−2186.